Journal of the Korean Society for Nondestructive Testing
Vol. 23, No. 3 (2003. 6)

Virtual Reality Presentation of Moment Tensor Analysis by SiGMA

Masayasu Ohtsu*,† and Mitsuhiro Shigeishi**

Abstract Nucleation of a crack is readily detected by acoustic emission (AE) method. One powerful technique for AE waveform analysis has been developed as SiGMA (Simplified Greens functions for Moment tensor Analysis), as crack kinematics of locations, types and orientations are quantitatively determined. Because these kinematical outcomes are obtained as three-dimensional (3-D) locations and vectors, 3-D visualization is definitely desirable. To this end, the visualization system has been developed by using VRML (Virtual Reality Modeling Language). As an application, failure process of a reinforced concrete beam is discussed.

Keywords: acoustic emission, moment tensor analysis, reinforced concrete beams, visualization, virtual reality

1. Introduction

The generalized theory of acoustic emission (AE) has been established on the basis of elastodynamics (Ohtsu and Ono, 1984). Thus, it is clarified that AE waves are elastic waves due to dynamic dislocation in a solid. Theoretical treatment of AE in concrete was studied as elastic waves in a homogeneous medium (Ohtsu, 1982). The results were remarkably successful, whereas concrete is not homogeneous but heterogeneous. This is because elastodynamic properties of material constituents are physically dependent on the relation between the wavelengths and the characteristic dimensions of heterogeneity. In the case that the wavelengths are even larger than the sizes of heterogeneous inclusions, the effect of heterogeneity is inconsequent. This is the case of massive solids such as concrete and rock, if the sizes of specimens are large enough compared with the wavelengths.

Theoretical treatment of AE waves leads to the moment tensor analysis for source kinematics (Kim and Sachse, 1984) and the deconvolution analysis for kinetics (Hsu and Hardy, 1978). In the former paper, only diagonal components of the moment tensor were assumed to characterize cracking mechanisms of glass due to indentation. Mathematically, the presence of tensor components is not actually associated with the type of the crack, but substantially related with the coordinate system. Although the crack orientations are often assumed as parallel to the coordinate system (Saito, Takemoto, Suzuki and Ono, 1998), they are generally inclined to the coordinate system mostly because of the configuration of the specimen. As a result, the presence of all the components is consequent whether the type of the crack is of tensile or of shear.

In order to perform the moment tensor analysis, one powerful technique for AE waveform analysis has been developed as

Received April 19, 2003, Accepted June 5, 2003. * Graduate School of Science and Technology, Kumamoto University, 2-39-1 Kurokami, Kumamoto 860-8555, Japan, ** Department of Civil Engineering and Architecture, Kumamoto Univ., † Corresponding author: ohtsu@gpo.kumamoto-u.ac.jp

SiGMA (Simplified Green's functions for Moment tensor Analysis) (Ohtsu, 1991). Crack kinematics on locations, types and orientations are quantitatively determined. Because these kinematical outcomes are obtained as three-dimensional (3-D) locations and vectors, 3-D visualization of results is desirable. To this end, the visualization procedure has been developed by using VRML (Virtual Reality Modeling Language).

Theoretical Background

An elastodynamic solution of wave motions $\mathbf{u}(\mathbf{x},t)$ is mathematically represented as,

$$u_k(\mathbf{x},t) = \int_S [G_{ki}(\mathbf{x},\mathbf{y},t)*t_i(\mathbf{y},t) - T_{ki}(\mathbf{x},\mathbf{y},t)*u_i(\mathbf{y},t)]dS \quad (1)$$

where $\mathbf{u}(\mathbf{x},t)$ and $\mathbf{u}(\mathbf{y},t)$ are displacements, and $\mathbf{t}(\mathbf{y},t)$ are tractions. The asterisk * represents the convolution integral in time. $G_{ik}(\mathbf{x},\mathbf{y},t)$ are Green's functions and $T_{ik}(\mathbf{x},\mathbf{y},t)$ are the associated tractions with Green's functions,

$$T_{ik}(\mathbf{x},\mathbf{y},t) = G_{ip,q}(\mathbf{x},\mathbf{y},t)\ C_{pqjk}\ n_j \quad (2)$$

Here C_{pqjk} are the elastic constants, and $G_{ip,q}(\mathbf{x},\mathbf{y},t)$ are the spatial derivatives of Green's functions as they imply $\partial G_{ip}(\mathbf{x},\mathbf{y},t)/\partial x_q$. $\mathbf{n}$ is the unit normal vector to the boundary surface S. Physical meaning of Green's function is readily derived, as applying one force, $\mathbf{t}(\mathbf{y},t) = \mathbf{f}(\mathbf{y},t)$, at only one point $\mathbf{y}$ on the boundary S and eq. (1) is converted as,

$$u_i(\mathbf{x},t) = G_{ij}(\mathbf{x},\mathbf{y},t)*f_j(\mathbf{y},t) \quad (3)$$

Thus, $G_{ij}(\mathbf{x},\mathbf{y},t)$ results in the dynamic displacement $u_i(\mathbf{x},t)$ in the x_i direction at point $\mathbf{x}$ due to the force $f_j(\mathbf{y},t)$ in the x_j direction at point $\mathbf{y}$. Because Green's functions are dependent on not only material properties but also on configuration of the medium, they have to be computed numerically. Only for an infinite space, analytical solutions are known. Semi-analytical solutions were already reported in a half space (Ohtsu and Ono, 1984) and in an infinite plate (Pao and Ceranoglu, 1981). For a finite body, numerical solutions of Green's functions were reported by applying the finite element method (Hamstad, O'Gallagher and Gary, 1999).

A famous experiment of pencil-lead break (Hsu and Hardy, 1978) is mathematically represented by eq. (3). A pencil-lead break is known to generate Heaviside's step-function force, $H(t)e_j(\mathbf{y})$, where $\mathbf{e}(\mathbf{y})$ is the unit direction vector at point $\mathbf{y}$. Since the convolution with the step function leads to the integration in time, eq. (3) becomes,

$$p_i(\mathbf{x},t) = \int G_{ij}(\mathbf{x},\mathbf{y},t)e_j(\mathbf{y})\ dt \quad (4)$$

Here $p_i(\mathbf{x},t)$ is the detected waveform by the displacement sensor. Accordingly, Green's function of an arbitrary specimen, $G_{ij}(\mathbf{x},\mathbf{y})$, can be empirically obtained from,

$$G_{ij}(\mathbf{x},\mathbf{y},t) = dp_i(\mathbf{x},t)/dt \quad (5)$$

It is noted that the orientation of AE sensor sensitivity is parallel to the x_i-direction and the force due to pencil-lead break is released in the x_j-direction.

Although some attempts were carried out to apply these Green's functions to the source characterization of AE, eq. (3) cannot be applied to AE waves due to cracking. In seismology, fault (cracking) mechanisms are represented by such equivalent forces as dipole and couple forces. The dipole forces are known as two forces of the same magnitude and the opposite directions on the coincident straight line. The couple forces are two parallel and opposite-direction forces with infinitesimal distance. In order to combine these forces with empirical Green's functions, the pencil-lead break

must be generated in the directions that are associated with the orientations of these forces. If the dipole forces or the couple forces are applied in the two opposite directions at the same location, actually resultant Green's functions lead to no motions.

In order to model a crack as an AE source, the boundary surface **S** in eq. (1) is replaced by internal surface F of a crack surface. To introduce the discontinuity of displacements (dislocation), virtual two surfaces F^+ and F^- are considered as shown in Fig. 1. Before a crack is nucleated, these two surfaces make a coincident motion. Due to cracking, the discontinuity of displacement $\mathbf{b}(\mathbf{y},t)$ is nucleated between the two surfaces and denoted by using superscripts + and - on surface F^+ and F^-,

$$b_i(\mathbf{y},t) = u_i^+(\mathbf{y},t) - u_i^-(\mathbf{y},t) \tag{6}$$

Vector $\mathbf{b}(\mathbf{y},t)$ is called the dislocation and is identical to Burgers vector in crystallography. Setting $\mathbf{t}(\mathbf{y},t) = 0$ on the surface F, eq. (1) is rewritten,

$$\begin{aligned} u_k(\mathbf{x},t) = & \int_{F^+}[- T_{ki}^+(\mathbf{x},\mathbf{y},t)*u_i^+(\mathbf{y},t)]dF \\ & + \int_{F^-}[- T_{ki}^-(\mathbf{x},\mathbf{y},t)*u_i^-(\mathbf{y},t)]dF \end{aligned} \tag{7}$$

where T_{ik}^+ and T_{ik}^- contain the normal vector $\mathbf{n}^+$ and $\mathbf{n}^-$, respectively. Assuming $\mathbf{n} = \mathbf{n}^+ = -\mathbf{n}^-$, and $F = F^-$,

$$\begin{aligned} u_k(\mathbf{x},t) &= -\int_F T_{ki}(\mathbf{x},\mathbf{y},t)*[-u_i^+(\mathbf{y},t)]]dF \\ &\quad + \int_F[- T_{ki}(\mathbf{x},\mathbf{y},t)*[u_i^-(\mathbf{y},t)]dF \\ &= \int_F T_{ki}(\mathbf{x},\mathbf{y},t)*[u_i^+(\mathbf{y},t)-u_i^-(\mathbf{y},t)]dF \\ &= \int_F T_{ki}(\mathbf{x},\mathbf{y},t)*b_i(\mathbf{y},t)dF \end{aligned} \tag{8}$$

Comparing eq. (3) with eq. (8), it is understandable that Green's functions empirically obtained from the pencil-lead break can not be applied to AE waves due to cracking. Based on eq. (2), eq. (8) is converted as,

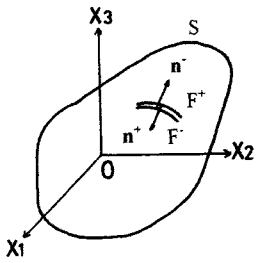

Fig. 1 Crack (dislocation) surfaces F+ and F-.

$$\begin{aligned} u_k(\mathbf{x},t) &= \int_F T_{ki}(\mathbf{x},\mathbf{y},t)*b_i(\mathbf{y},t)\ dF \\ &= \int_F G_{kp,q}(\mathbf{x},\mathbf{y},t)\ C_{pqij}\ n_j*b_i(\mathbf{y},t)dF \\ &= G_{kp,q}(\mathbf{x},\mathbf{y},t)*S(t)\ C_{pqij}\ n_j l_i \int_F b(\mathbf{y},t)dF \\ &= G_{kp,q}(\mathbf{x},\mathbf{y},t)*S(t)\ C_{pqij}\ n_j l_i DV \end{aligned} \tag{9}$$

where **l** is the unit direction vector and S(t) is the source-time function of crack motion. DV is the crack volume. It is noted that the amplitude of AE wave, $\mathbf{u}(\mathbf{x},t)$, is explicitly associated with the crack volume, neither simply with the crack area nor with crack opening. This implies that some attempts to determine the crack area or the magnitude of shear slip (Enoki, Kishi and Kohara, 1986: Dai, Labuz and Carvalho, 2000) were not rational, because only a disk-shaped crack was taken into account. According to the simulation analysis (Ohtsu, Yuyama and Imanaka, 1987), the crack volume estimated as the penny-shaped crack was more than 30% different from that of the disk-shaped. Equation (9) is the theoretical representation of AE wave due to cracking and can be available for simulation analysis (Ohtsu, 1982).

SiGMA Analysis

Since eq. (9) is fairly complicated and contains two vectors **l** and **n**, moment tensor M_{pq} is introduced for an inverse problem,

$$M_{pq} = C_{pqkl} l_k n_l\ DV \tag{10}$$

Then, eq. (9) is rewritten as,

$$u_k(\mathbf{x},t) = G_{kp,q}(\mathbf{x},\mathbf{y},t)\ M_{pq}*S(t) \qquad (11)$$

According to eq. (10), the moment tensor, M_{pq}, is defined by the product of the elastic constants [N/m^2] and the crack volume [m^3], which leads to the moment of physical unit [Nm]. In the case of an isotropic material,

$$M_{pq} = ll_k n_k\ dpq + m(l_p n_q + l_q n_p)DV \qquad (12)$$

where l and m are Lame's elastic constants. Originally, the seismic moment, mbDF [Nm], wa defined as the product of shear modulus m [N/m^2], shear displacement b [m], and area of fault DF [m^2]. Setting **l** = (1, 0, 0), **n** = (0, 1, 0) (**l** is perpendicular to **n**) and DV = bDF in eq (12), one component M_{12} is obtained as 2mbDF which is obviously equivalent to the seismic moment. This is the reason why the tensor is named as the moment tensor. Equation (12) leads to the fact that the moment tensor is comparable to a stress due to crack nucleation, as a symmetric second-order tensor as shown in Fig. 2.

Mathematically, such equivalent forces as the dipole forces and the double-couple forces correspond to particular components of the stress in Fig. 2. Normal components of the moment tensor are identical to the dipole forces, while couple forces correspond to tangential (shear) components. The concept of the equivalent forces is so misleading that the nucleation of a tensile crack is represented by only a pair of dipole forces. In the case of a pure tensile crack, a scalar product $l_k n_k = 1$. Since all diagonal components contain the scalar product as given in eq. (12), the tensile crack should be modeled by three normal components (three pairs of dipole forces). In contrast, couple forces correspond to off-diagonal components in eq. (12). Since the moment tensor is symmetric, double-couple forces are rational.

For an inverse problem of eq. (11), the spatial derivatives of Green's functions are inevitably required. Accordingly, numerical solutions were obtained by FDM (Enoki, Kishi and Kohara, 1986) and by FEM (Hamstad, O'Gallagher and Gary, 1999). These solutions, however, need a vector processor for computation, and are not readily applicable to processing a large amount of AE waves. Based on the far-field term of P-wave, a simplified procedure has been developed, which is suitable for a PC-based processor and robust in computation. The procedure is now implemented as a SiGMA (Simplified Green's functions for Moment tensor Analysis) code. By taking account of only P wave motion of the far field (1/R term) of Green's function in an infinite space, the displacement $U_i(\mathbf{x},t)$ of P-wave motion is obtained from eq. (11) as,

$$U_i(\mathbf{x},t) = [-1/(4pv_p^3)](\ r_i r_p r_q/R)[dS(t)/dt]\ M_{pq} \qquad (13)$$

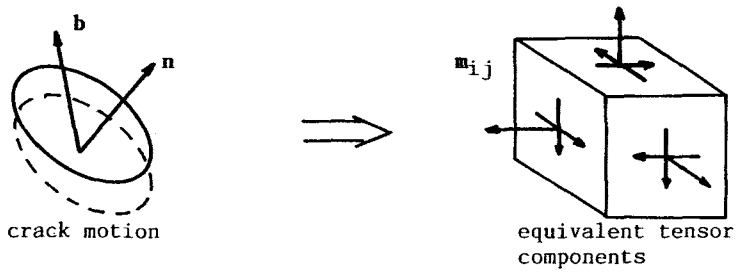

Fig. 2 Modeling crack motion by the moment tensor

Here ρ is the density of material and v_p is the velocity of P-wave. R is the distance between the source **y** and the observation point **x**, of which directional cosine is **r** = (r_1, r_2, r_3). Considering the effect of reflection at the surface and neglecting the source-time function, the amplitude A(**x**) of the first motion is represented as,

$$A(\mathbf{x}) = [C_s \; Ref(\mathbf{t},\mathbf{r})/R] \; r_i \; M_{ij} \; r_j \qquad (14)$$

where C_s is the calibration coefficient including material constants in eq. (13) and **t** is the direction of the sensor sensitivity. Ref(**t**,**r**) is the reflection coefficient at the observation location **x**. In the relative moment tensor analysis (Dahm, 1996), this coefficient is not taken into consideration, because the effect of the sensor locations is compensated. Since the moment tensor is symmetric, the number of independent unknowns M_{ij} to be solved is six. Thus, multi-channel observation of the first motions at more than six channels is required to determine the moment tensor components.

Displaying AE waveform on CRT screen, two parameters of the arrival time (P1) and the amplitude of the first motion (P2) in Fig. 3 are determined. In the location procedure, source location **y** is determined from the arrival time differences. Then, distance R and its direction vector **r** are determined. The amplitudes of the first motions at more than 6 channels are substituted into eq. (14), and the components of the moment tensor M_{ij} are determined. Since the SiGMA code requires only relative values of the moment tensor components, the relative calibration of the sensors is sufficient. Then, the classification of a crack is performed by the eigenvalue analysis of the moment tensor. Setting the ratio of the maximum shear contribution as X, three eigenvalues for the shear crack become X, 0, -X. Likewise, the ratio of the maximum deviatoric tensile component is set as Y and the isotropic tensile as Z. It is assumed that the principal axes of the shear crack are identical to those of the tensile crack. Then, the eigenvalues of the moment tensor for a general case are represented by the combination of the shear crack and the tensile crack. Because relative values are determined in the SiGMA, three eigenvalues are normalized and decomposed,

$$\begin{aligned} 1.0 &= X + Y + Z \\ \text{the intermediate eigenvalue/the maximum eigenvalue} &= 0 - Y/2 + Z \\ \text{the minimum eigenvalue/the maximum eigenvalue} &= -X - Y/2 + Z \end{aligned} \qquad (15)$$

where X, Y, and Z denote the shear ratio, the deviatoric tensile ratio, and the isotropic tensile ratio, respectively. In the present SiGMA code, AE sources of which the shear ratios are less than 40% are classified into tensile cracks. The sources of X > 60% are classified into shear cracks. For X values between 40% and 60%, cracks are referred to as mixed mode. In the eigenvalue analysis, three eigenvectors **e1**, **e2**, and **e3**,

$$\begin{aligned} \mathbf{e1} &= \mathbf{l} + \mathbf{n} \\ \mathbf{e2} &= \mathbf{l} \times \mathbf{n} \\ \mathbf{e3} &= \mathbf{l} - \mathbf{n} \end{aligned} \qquad (16)$$

are also determined. Vectors **l** and **n**, which are interchangeable, are recovered from eq. (16).

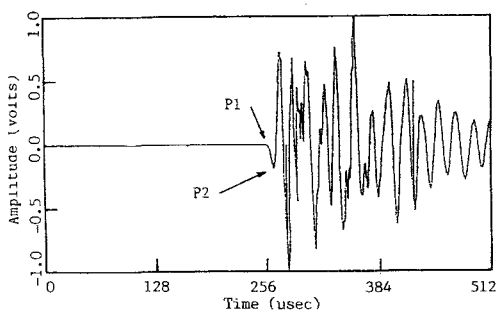

Fig. 3 Detected AE wave and two parameters P1 and P2

Three-Dimensional Visualization by VRML

Visualization procedure has been developed by using VRML (Virtual Reality Modeling Language). By applying a conventional SiGMA code, analytical results for one AE event are listed in Table 1. From the top, event number, moment tensor components and the location of AE source in the Cartesian coordinates are denoted. Following normalized eigenvalues, three eigenvectors and X (Shear), Y(CLVD) and Z(Mean) ratios are given. Here, deviatoric component Y is referred to as a compensated linear-vector dipole (CLVD) after Knopoff and Randall (1970). At the bottom line, crack motion vector **l** and crack normal vector **n** are shown, which are interchangeable.

Table 1 Listed results of SiGMA analysis

```
[-] Event Number : 25

[-] Moment Tensor Solution
    ************************
    0.4526  0.1073   0.0543
            0.1151   0.5543
                     1.0000
    ************************

[-] Source Location Solution
     X       Y       Z
    -0.015  -0.029   0.012

[-] Eigen Values & Vectors Solution
                        maximum  intermediate  minimum
    Eigen Value     |    1.0000   -0.0865    -0.3905
    Eigen Vector X  |   -0.0014    0.3308    -0.9437
    Eigen Vector Y  |   -0.4336   -0.8506    -0.2975
    Eigen Vector Z  |   -0.9011    0.4088     0.1446
    Composition Ratio of Eigen Value (%)
    Shear : 30.40  |  CLVD :   52.16  |  Mean :   17.43

[-] Crack Motion & Crack Surface Normal Directions
            X       Y       Z
    Motion -0.443  -0.522  -0.729
    Normal  0.440  -0.244  -0.864
```

These data are, for example, currently plotted as shown in Fig. 4. AE events are displayed at their locations with symbols. A tensile crack is denoted by arrow symbol, of which direction is identical to that of crack opening. A shear crack is denoted by cross symbol, of which two directions correspond to the two vectors **l** and **n**. As can be seen, classification of cracks is readily made, whereas crack orientation is not easily recognized. This is because two-dimensional plotting is adopted and results are inherently suitable for three-dimensional visualization. In this respect, VRML has been introduced. Crack modes of tensile, mixed-mode and shear are given in Fig. 5. Here, an arrow vector indicates the crack motion vector, and a circular plate corresponds to the crack surface, which is perpendicular to the crack normal vector.

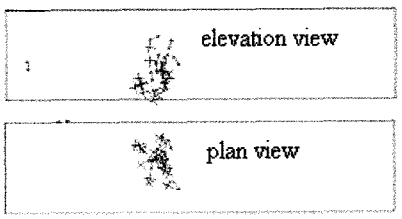

Fig. 4 Results plotted in SiGMA analysis

(a) tensile crack

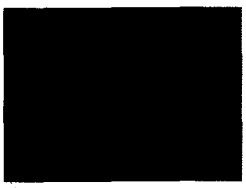

(b) shear crack

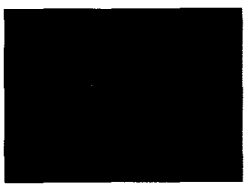

(c) mixed-mode

Fig. 5 3-D display models for tensile, shear and mixed-mode cracks

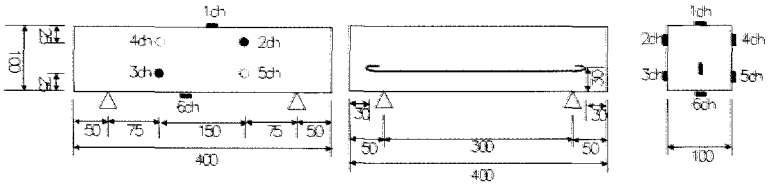

Fig. 6 Specimen and sensor array

Experimental Results and Discussion

Experiments were conducted by using reinforced concrete beams of dimensions 10 cm x 10 cm x 40 cm. One rebar of 10 mm diameter was arranged at 30 mm cover-thickness. Compressive strength of concrete was 33.4 MPa at 28 days. Modulus of elasticity and the velocity of P wave were 24 GPa and 3140 m/s, respectively. Six AE sensors were attached to the specimen. The locations of sensors and the configuration of a reinforced concrete beam are shown in Fig. 6.

The specimen was loaded as shown in Fig. 7. Bending failure of the reinforced concrete beam was generated. Without reinforcement, concrete beams suddenly break into two pieces when the stress at the bottom side reaches the tensile strength. Sudden crack propagation from the bottom to the top is prevented with reinforcement. As a result, failure process is visually divided into several stages.

Tensile cracks are generated first at the bottom region as bending cracks. Then, delamination between the concrete and the reinforcement occurs. Along with this failure, bending cracks grow further. The tips of cracks extend upward, penetrating into the compressive zone of the upper half. The cracks may stop at this stage due to compression, and the beam reaches final failure of diagonal-shear failure or concrete crashing at the upper half.

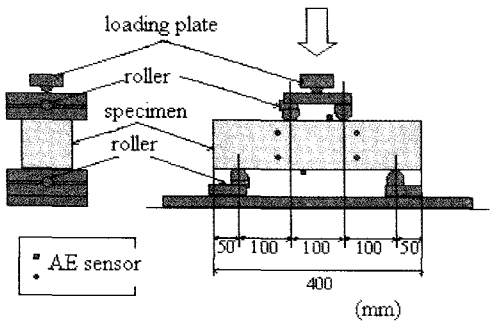

Fig. 7 Experimental set-up

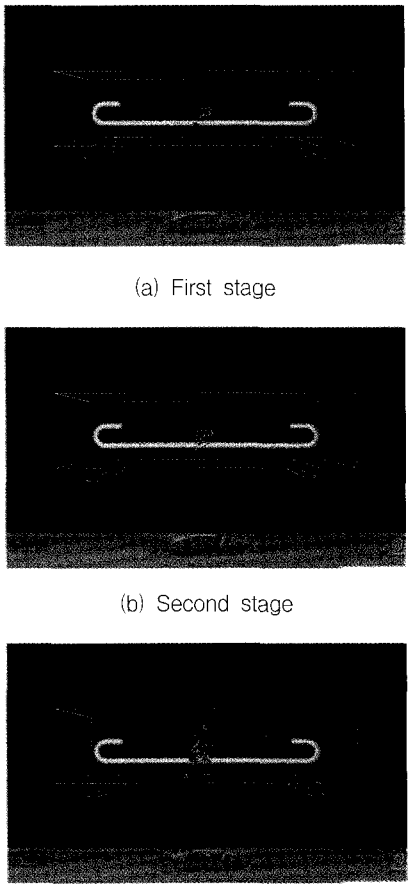

(a) First stage

(b) Second stage

(c) Third stage

Fig. 8 Results of SiGMA analysis on the beginning three stages

3-D visualization of SiGMA analysis on the beginning three stages is given in Fig. 8. At the first stage, a few tensile cracks (green) and mixed-mode cracks (red) are mostly observed near reinforcement at the central region. Activity of cracking increases at the second stage as the increase of mixed-mode cracks. At this stage, bending cracks are visually observed. At the third stage, AE cluster expands upward, increasing the number of shear cracks (blue).

The latter two stages are shown in Fig. 9. Cluster of AE sources further expands and the nucleation of cracks is really mixed up of tensile, mixed-mode, and shear cracks. It is noted that tensile and mixed-mode cracks are intensely observed around reinforcement, while shear cracks are particularly observed at the compressive zone. At the fifth stage, cracks distribute widely, probably corresponding to the nucleation of diagonal shear cracks between the loading point and the support.

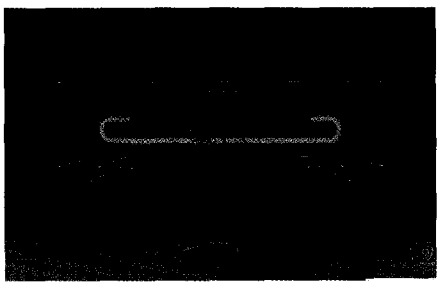

(a) Fourth stage

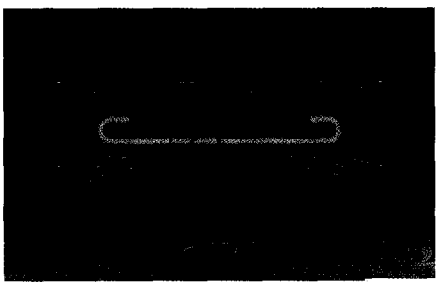

(b) Fifth stage

Fig. 9 Results of SiGMA analysis on the last two stages

Combining all results analyzed, Fig. 10 is obtained. As shown, all figures are actually movable and rotatable. Therefore, locations and orientations of the source can be visually identified. This is a merit of 3-D visualization by means of VRML.

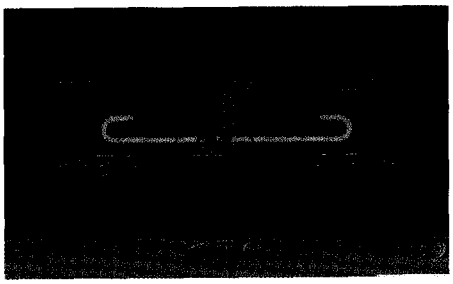

(a) All the data plotted

(b) Visualization from an inclined angle

Fig. 10 Results of all the data analyzed

Conclusion

Nucleation of cracks can be quantitatively analyzed from AE waveforms, by applying SiGMA (Simplified Green's functions for Moment tensor Analysis) code. Crack kinematics on locations, types and orientations are determined three-dimensionally. Because visualization of results is desirable, three-dimensional visualization procedure for SiGMA analysis is developed by using VRML (Virtual Reality Modeling Language). As a case study, failure process of a reinforced concrete beam is successfully visualized and discussed.

References

Dai, S. T., Labuz, J. F. and Carvalho, F. (2000) Softening Response of Rock Observed in Plane-Strain Compression, *Trends in Rock Mechanics*, Geo SP-102, ASCE, pp. 152-163.

Dahm, T. (1996) Relative Moment Tensor Inversion based on Ray Theory: Theory and Synthetic Tests, *Geophys. J. Int.*, No. 124, pp. 245-257.

Enoki, M., Kishi, T. and Kohara, S. (1986) Determination of Micro-cracking Moment Tensor of Quasi-cleavage Facet by AE Source Characterization, *Progress in Acoustic Emission III*, JSNDI, pp. 763-770.

Hamstad, M. A., O'Gallagher, A. and Gary, J. (1999) Modeling of Buried Monopole and Dipole Source of Acoustic Emission with a Finite Element Technique, *Journal of Acoustic Emission*, Vol.17, No. (3-4), pp. 97-110.

Hsu, N. N. and Hardy, S. C. (1978) Experiments in AE Waveform Analysis for Characterization of AE Sources, Sensors and Structures, *Elastic Waves and Nondestructive Testing of Materials*, AMD-Vol. 29, pp. 85-106.

Kim, K. Y. and Sachse, W. (1984) Characterization of AE Signals from Indentation Cracks in Glass, *Progress in Acoustic Emission II*, JSNDI, pp. 163-172.

Knopoff, L. and Randall, M. J. (1970) The Compensated Linear-Vector Dipole : A Possible Mechanism for Deep Earthquakes, *Journal of Geophysical Research*, Vol. 75, No. 26, pp. 4957-4963.

Ohtsu, M. (1982) Source Mechanism and Waveform Analysis of Acoustic Emission in Concrete, *Journal of Acoustic Emission*, Vol. 2, No. 1, pp. 103-112.

Ohtsu, M. and Ono, K. (1984) A Generalized Theory of Acoustic Emission and Green's Functions in a Half Space, *Journal of Acoustic Emission*, Vol. 3, No. 1, pp. 124-133.

Ohtsu, M., Yuyama, S. and Imanaka, T. (1987) Theoretical Treatment of Acoustic Emission Sources in Microfracturing due to Disbonding, J. *Acoust. Sco. Am.*, Vol. 82, No. 2, pp. 506-512.

Ohtsu, M. (1991) Simplified Moment Tensor Analysis and Unified Decomposition of Acoustic Emission Source: Application to In Situ Hydrofracturing Test, *Journal of Geophysical Research*, Vol. 96(B4), pp. 6211-6221.

Ohtsu, M. and Ohtsuka, M. (1998) Damage Evolution by AE in the Fracture Process Zone of Concrete, *J. Materials, Conc. Struct. Pavement*, JSCE, No. 599/V-40, pp. 177-184.

Pao, Y. H. and Ceranoglu, A. N. (1981) Propagation of Elastic Pulse and Acoustic Emission in a Plate, *J. Appl. Mech.*, Vol. 48, pp.125-147.

Saito, N., Takemoto, M., Suzuki, H. and Ono, K. (1998) Advanced AE Signal Classification for Studying the Progression of Fracture Modes in Loaded UD-GFRP, *Progress in Acoustic Emission IX*, JSNDI, pp. V-1 - V-10.